Global NEST Journal, Vol 27, No X, pp 1-10
Copyright© 2025 Global NEST
Printed in Greece. All rights reserved

Synergistic Effects of Co-pyrolysis of Nylon6 and Cotton on Cr(VI) Adsorption

Xingjie Zhao^A, Yixiao Zhang^A, Yuyan Liu^A, Teng Wang^A,B, Jingxin Liu^A,B, Meng Mei^A,B, Wenxia Wang^A,B and Si Chen^A,B*
^A School of Resources and Environment, Wuhan Textile University, Wuhan 430073, China
^B Engineering Research Centre for Clean Production of Textile Dyeing and Printing, Ministry of Education, Wuhan Textile University, Wuhan 430073, China

Received: 06/09/2024, Accepted: 21/06/2025, Available online: 10/12/2025

*to whom all correspondence should be addressed: e-mail: 2019098@wtu.edu.cn

https://doi.org/10.30955/gnj.06780

Graphical abstract

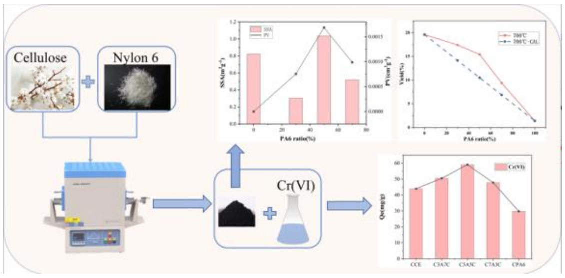

Abstract

Recycling of used textiles is an important part of achieving sustainable development and low carbon, which can effectively alleviate environmental pollution and improve waste reuse, but the recycling management of blended textiles is particularly challenging. Blends of Nylon6 and cotton are increasingly popular in high-value textile applications, but the issue of recycling and disposal has yet to be resolved. Cotton and polyamide 6 at varying weight percentages were co-pyrolyzed in this study, and the co-pyrolysis process was evaluated using a Synchronized Thermal Analyzer (TG-DSC) to determine the synergistic effect of the two. The synergistic effect greatly contributes to the output of biochar, increasing the specific surface area and pore volume of biochar, thereby enhancing the adsorption capacity of the resulting char for Cr(VI). when the polyamide 6 ratio is 50%, the char has the highest adsorption capacity on Cr(VI). The physicochemical features of co-pyrolytic char were investigated using SEM-EDS, XPS, BET, and FTIR to determine the synergistic mechanism. Overall, cotton and polyamide 6 exhibit apparent synergistic effect in the co-pyrolysis process, providing char with extraordinary adsorption capability.

Keywords: mixed textiles, co-pyrolysis, cotton, nylon 6, synergistic effect

1. Introduction

The textile industry is one of the world's largest and oldest, but it faces a number of environmental difficulties and challenges, from textile processing to final disposal (Kasavan *et al.* 2021). The disposal of products at the end of their service life is a major environmental concern in the textile industry (Stanescu 2021). Globally, 87% of waste textiles are landfilled or burnt each year, resulting in huge economic losses (Espinoza Pérez *et al.* 2022).

The annual production of waste textiles in the U.S., EU and China exceeds 49 kg, 5.8 million tons and 1 million tons respectively, and is growing rapidly at a rate of more than 10% per year. (Holland *et al.* 2018; Lu *et al.* 2022). As a result, effective textile solid waste management is required to ensure the textile industry's long-term development (Kankia *et al.* 2021; Kankia *et al.* 2021).

Textile production is very complex, and the fiber raw materials mainly include natural and synthetic fibers (Mohd Hanafiah *et al.* 2024; Mohd Hanafiah *et al.* 2024). Cotton is one of the most extensively used textile materials and is typically combined with other natural fibers, chemical fibers such as polyester, polyurethane, and polyamide, as well as pure cotton textiles (Haslinger *et al.* 2019). Currently, the most frequent waste textile treatment procedures are recycling, incineration, and landfill, and recycled waste textiles are eventually processed by incineration or landfill (To *et al.* 2019). Incineration recycles energy, chemical byproducts, and oil byproducts, but produces toxic gases such as dioxins, polycyclic aromatic hydrocarbons (PAHs), and polychlorinated biphenyls (PCBs), which are hazardous to ecosystems and human health, and result in the waste of large amounts of natural materials (Kumar and Samadder 2017). As a result, pyrolysis is utilized as an alternative to incineration to maximize the economic benefits of recycling waste textiles (Sayed *et al.* 2021, 2022).

Pyrolysis is a thermochemical process that turns heterogeneous and complicated waste materials into value-added products (also known as waste upcycling) (Lee *et al.* 2023). Currently, researchers create biochar by pyrolyzing waste textiles such as cotton, polyester, and acrylics and performing various modifications on them, which is used as an adsorbent material for the adsorption

Xingjie Zhao, Yixiao Zhang, Yuyan Liu, Teng Wang, Jingxin Liu, Meng Mei, Wenxia Wang and Si Chen (2025), Synergistic Effects of Co-pyrolysis of Nylon6 and Cotton on Cr(VI) Adsorption, *Global NEST Journal*, **27**(XX), 1-10.

of heavy metals and pigments in polluted water (Sayed *et al.* 2024).

Co-pyrolysis can take advantage of the respective strengths of the two raw materials to complement and optimize resources, thus achieving the purpose of waste for waste (Han *et al.* 2022). Co-pyrolyzing the sludge with the biomass improves the quality of the biochar, accelerates the breakdown of the mixture, and lowers the reaction temperature (Dai *et al.* 2022). Shrimp shells and corn stover were co-pyrolyzed to reduce energy usage and increase the breakdown of $CaCO_3$(Liu *et al.* 2021). When beech wood is pyrolyzed in combination with polyamide-6, the pyrolysis products (biochar, liquids and gases) show a new combination of forms (de Rezende Locatel *et al.* 2022). The above studies all indicate that there is interaction between the two raw materials during co-pyrolysis. In practical applications, most of the waste textiles used for pyrolysis and resource utilization are blended textiles, and the polymers in blended raw materials also interact during the cracking process (Hanoğlu *et al.* 2019).

The development of industry has caused a series of environmental problems, and heavy metal pollution in wastewater is particularly prominent. Chromium accumulates in large quantities in the environment, and chromium in wastewater mainly exists in the form of Cr(III) and Cr(VI), of which Cr(VI) is more harmful (Zhang *et al.* 2018). Among the many methods for Cr(VI) removal, the adsorption method is widely cited for its high adsorption capacity and low operating cost (Y. Wang *et al.* 2020). The low cost and environmental friendliness of biochar-based materials are commonly used in adsorption treatments (Zeng *et al.* 2021).

Polyamide 6 (PA6) is a chemical fiber fabric with exceptional chemical and abrasion resistance, second only to polyester, and is commonly mentioned in the textile industry; however, its non-biodegradable qualities make it difficult to disintegrate in the natural environment. Nylon6 and cotton blends, a high value-added fabric popular in recent years, are wear-resistant and washable, with superior shape retention and warmth, smooth and easy-to-clean surfaces, but the separation process is hard.

Currently, the synergistic mechanism of cotton-nylon blends in the co-pyrolysis process has not been fully elucidated in existing studies and still needs to be further explored; the mechanism of the effect of different blending ratios on the pyrolytic carbon has not been determined within a clear theoretical framework either. (Xu *et al.* 2019). Therefore, this study is of great significance for the research on the co-pyrolysis of blended textiles. We tried to use TG-DSC to investigate the co-pyrolysis effect of different mixing ratios of brocade cotton, and evaluated the removal of Cr(VI) by the co-pyrolysis carbon under the optimal ratios, which finally proved the real existence of the synergistic effect.

2. Materials and methods

2.1. Materials

CE (cellulose powder) is the main component of cotton (cotton fibers contain more than 90% cellulose), and its chemical structure (β-1,4-glycosidic bond) is the same as that of cotton.PA6 (polyamide 6 powder) is a purified form of synthetic nylon 6, and has the exact same chemical structure (amide bond) as nylon 6. Experimentally, pure CE and pure PA6 were used to replace pure cotton and nylon, which were mixed thoroughly with a mortar and pestle to prepare blended samples with different ratios (3/7, 5/5, 7/3) labelled as CE, PA6, 3A7C, 5A5C, 7A3C, respectively. $K_2Cr_2O_7$, HCl, HNO_3 and NaOH were analytically pure reagents. All solutions were configured with deionized water (18.25 mΩ/cm).

2.2. Method

2.2.1. TG-DSC analysis

Synchronized thermal analyzer (TG-DSC) can provide TG and DSC signals simultaneously. The empty crucible was weighed on a balance, and 10 mg of the sample was loaded into the crucible and heated from 50°C to 800°C at an elevated temperature rate of 10 °C/min with an inert gas (N_2) flow rate of 60 mL/min. The TG-DSC instrument was calibrated using standard indium (melting point 156.6°C, ΔH=28.45 J/g) prior to the experiment to ensure the accuracy of the thermal analysis data.

2.2.2. Preparation of biochars

The different mixed samples were placed in quartz crucibles and then placed in a tube furnace and heated from 50°C to 700°C under N_2 and held for 1h. The cooled samples were removed from the tube furnace and the pyrolyzed carbon yields of the solid residues were calculated and named as CCE, CPA6, C3A7C, C5A5C, C7A3C and retained for further experiments. The specific process is shown in **Figure 1**. Thermocouples were passed through a standard temperature source to calibrate the temperature of the pyrolysis unit, and the gas flow rate was calibrated with a flow meter.

Figure 1. Diagram of pyrolysis unit

2.2.3. Removal of Cr(VI)

A 0.015 g portion of biochar was weighed and mixed with 30 mL Cr(VI) (100 mg/L) in a conical flask and put into a shaker at 150 rpm. Cr(VI) reacts with 1,5-diphenylcarbazide to form a pink complex. Cr(VI) after the reaction can be determined by UV-visible spectrophotometer, and the total chromium concentration can be determined by atomic absorption flame method. To ensure the accuracy of the experimental results, the experiment was repeated three times, and the average value was taken as the final result. The adsorption amount of Cr(VI) was calculated by equation (1).

$$q_e = \left(C_1 - C_2\right) \times V / m \tag{1}$$

C1 and C2 represent the initial and equilibrium concentrations of the solution (mg/L); V represents the volume of the solution (L); m represents the mass of biochar (g).

Weigh 0.015 g biochar into a 50 mL centrifuge tube, add 30 mL of Cr(VI) solution (100 mg/L), place it in a constant-temperature shaking incubator, and start the experiment and timing. Samples were taken at shaking times of 30 min, 60 min, 90 min, 120 min, 180 min, 240 min, 360 min, 480 min, 720 min, and 1440 min. The supernatant was filtered using a 0.45 µm filter membrane, and the concentrations of total Cr and Cr(VI) were measured separately. The experimental data were fitted using the first-order kinetic model, second-order kinetic model, and intra-particle diffusion model. The mathematical formulas for the kinetic models are as follows (Liu *et al.* 2020):

Pseudo-first-order (PFO) model

$$q_t = q_e\left(1 - e^{-k_1 t}\right) \tag{2}$$

Pseudo−second−order (PSO)mode

$$q_t = q_e - \frac{q_e}{k_2 q_e t + 1} \tag{3}$$

Intragranular diffusion model

$$q_t = k_i t^{0.5} + C \tag{4}$$

In the equation, q_t(mg/g) represents the adsorption capacity at time t, q_e(mg/g) denotes the adsorption capacity of biochar for Cr(VI) at adsorption equilibrium, k_1(1/min), k_2(g/(mg•min)), and ki(mg/(g•min$^{0.5}$)) represent the rate constants of the pseudo-first-order kinetic model, pseudo-second-order kinetic model, and intra-particle diffusion model, respectively, and C denotes the intercept related to the boundary thickness.

2.2.4. Zero-point charge determination

The isoelectric point is the pH value of the solution corresponding to the equilibrium of positive and negative charges carried by the adsorbent, at which time the adsorbent's surface charge is zero, showing electroneutrality, and the pH value of the solution at this time is recorded as pHpzc. Measure 30 mL of NaCl solution (0.1 mol/L) in a conical flask, weigh 0.015 g of biochar, adjust the initial pH of the solution by dropwise addition of HCl and NaOH, and determine the final pH by shaking for 24h. Use ΔpH to express the difference between the initial and final pH.

2.2.5. Characterization

SSA and PV of solid biochar were determined by nitrogen adsorption and Brunauer-Emmet-Teller (BET) method. Study of Weight Loss and Heat Change of Different Ratios of Nylon6 and Cotton Using Thermosynchronous Analyzer TG-DSC. Scanning electron microscopy (SEM) is used for the examination of the morphology and composition of materials. Fourier Transform Infrared Spectroscopy (FTIR) for Functional Group Analysis of Materials. Detection of elemental composition and valence distribution of biochar by X-ray photoelectron spectroscopy (XPS).

2.3. Data analysis

2.3.1. Heat of thermal decomposition

The heat of pyrolysis reaction is obtained by integrating the DSC curve as shown in equation (2)

$$Q = \int_0^t Q_P\, dt \tag{5}$$

where Q (kJ/kg) represents the heat of reaction, Q_P (mW/mg) and t are the DSC value and reaction time, respectively.

2.3.2. Synergetic effect calculation

The experimental value Y_{EXP} is obtained through equation (3). The synergistic effect can be expressed by Eq. (4), i.e., the difference between the experimental value and the theoretically calculated one. Synergies are positive when Y_{EXP} is greater than Y_{THE} (Mu *et al.* 2016).

$$Y_{THE} = \left(1-\gamma\right)Y_C + \gamma Y_A \tag{6}$$

$$\Delta TG = TG_{EXP} - TG_{THE} \tag{7}$$

where γ denotes the proportion of PA6 in the mixed sample, %; Y_C and Y_A are the TG/DTG values and pyrolysis solids yield of CE and PA6, respectively.

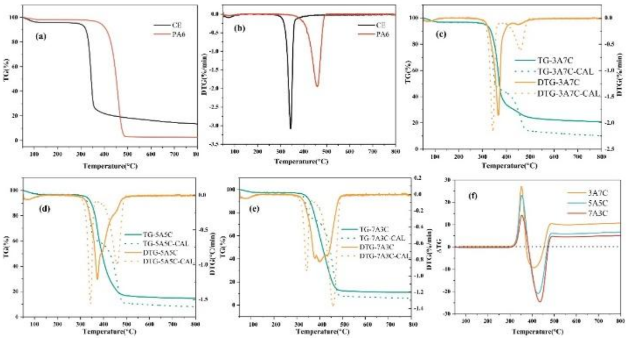

Figure 2. (a) TG; (b) DTG; (c-e) TG/DTG curves of co-pyrolysis; (f) ΔTG

3. Results and discussion

3.1. Analysis of the co-pyrolysis process

3.1.1. TG/DTG analysis

Figure 2(a-b) shows the pyrolysis process of CE and PA6 alone. The pyrolysis profile of CE is divided into three stages: initial decomposition, main decomposition and carbon decomposition as can be seen from the figure. When the pyrolysis temperature falls below 280°C, the physical properties of CE change, mainly by evaporation of water. 280-400°C is the main pyrolysis stage, the weight loss rate is as high as 67%, and a large number of pyrolysis products are produced, the main products include Ⅰ-glucose and various volatile gases, and the maximum weight loss rate occurs at 342.9°C (Sun *et al.* 2021; Zhu *et al.* 2004). Coke pyrolysis occurs above 430°C, a process in which dehydration and charring reactions compete with I-glucose production, and dehydration and charring reactions are more pronounced (Singh *et al.* 2021). PA6 undergoes thermal decomposition in the temperature range of 310-510°C, with the main mass loss being the formation of ε-caprolactam and other amines (Bozi *et al.* 2013). Weight loss up to 93 per cent, maximum rate of weight loss at 458.6°C, subsequent solid residues negligible (Perez *et al.* 2023).

3.1.2. The synergistic effect between CE and PA6

Co-pyrolysis experiments were carried out on the mixtures with different mixing ratio, and the TG/DTG experimental curves and theoretical calculated curves (calculated by equation 3) are shown in **Figure 2(c-e)**. From the experimental plots, it can be seen that the initial decomposition temperature of the blends is higher than that of pure cellulose, rising to 290°C, 292°C and 305°C as the PA6 content is varied from 30%, 50% and 70%, respectively. The theoretical calculation curve revealed that the pyrolysis section is made up of two major pyrolysis processes, and the single pyrolysis tests indicated above demonstrated that the weight loss temperature of CE is lower than that of PA6, and the degree of weight loss is different. Therefore, when the two substances are mixed (%) co-pyrolyzed at different weight ratios, a large difference between the theoretical and experimental curves occurs. In contrast, the pyrolysis phase of the experimental curve is influenced by PA6, with a weaker second pyrolysis phase. The actual weight loss temperature of the mixture was higher, but the weight loss rate tended to be inversely related to the percentage of PA6 added and was less than that of the two substances pyrolyzed separately. The synergistic effect of CE and PA6 resulted in discrepancies between experimental and theoretical values, which could be attributed to the fact that the nitrogen in the polyamide catalyzed the dehydration, decarboxylation, and carbonylation reactions but interfered with the generation of I-glucose, resulting in a higher fragmentation of the product and an increase in mass loss (Zhu *et al.* 2004).

3.1.3. DSC analysis

The heat flow (DSC, mW/mg) and heat of reaction (Q, kJ/kg) of the pyrolysis process are shown in **Figure 3**, with positive and negative representing exothermic and absorptive conditions, respectively (Dai, Liu, *et al.* 2022; X. Wang *et al.* 2016). From the DSC curves in **Figure 3(a)**, it is not difficult to see the trend of the heat required for co-pyrolysis. Heat flow changes were not significant for each material until 300°C. At temperatures between 300-800°C, the heat of reaction comes mainly from decomposition processes, including charring and volatilization, where charring is exothermic and volatilization is absorptive. (Ball *et al.* 2007; Rangasamy *et al.* 2021). The heat absorption peak of CE at 305-360°C corresponds to the production of I-glucose and various flammable gases (Sun *et al.* 2021). After 430°C, charring begins to dominate and leads to exothermic peaks. When mixed with PA6, volatilization of the aromatic ring dominates the decomposition, leading to a heat absorption process (Yang *et al.* 2007).

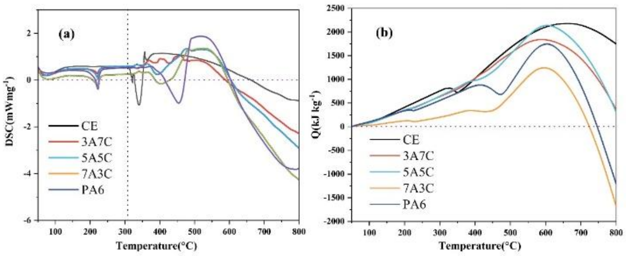

Figure 3. (a) Heat flow; (b) Reaction heat

From **Figure 3(b)**, it can be seen that the required heat for the pyrolysis of PA6 and CE alone, from 50°C to 800°C, is -1206.97 kJ/kg and 1746.95 kJ/kg, respectively. The heat absorption peak of PA6 at 360-500°C corresponds to the formation of ε-caprolactam and other amines with a heat demand of 899.99 kJ/kg. The heat absorption peak of CE at 300-360°C corresponds to the generation of Ⅰ-glucose and various combustible gases with a heat demand of 767.38 kJ/kg (Salman *et al.* 2019). At 400-700°C, the heat required in the co-pyrolysis process is related to PA6 (Dai, Liu, *et al.* 2022). 5A5C requires the highest heat demand, and the synergistic effect can be seen to be more prominent. Therefore, the synergistic effect is mainly caused by an exothermic reaction attributed to the cross-linking of CE with PA6(Bakirtzis *et al.* 2014).

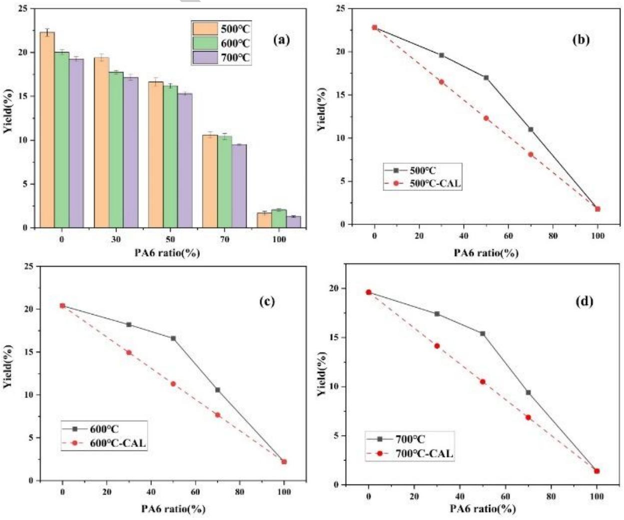

Figure 4. (a) Solid biochar yield; (b-d) theoretical vs. actual

3.1.4. Biochar yields

The solid char yields from co-pyrolysis at 500°C, 600°C and 700°C with different PA6 ratios are shown in **Figure 4**. The yield plots show that the carbon yield for CE solids only is about 20%, while the carbon yield for PA6 solids only is only 3% or less. The pyrolyzed carbon structure of PA6 consists of polycyclic aromatic hydrocarbons (PAH)(Bakirtzis *et al.* 2014). And the yield gradually decreases with increasing pyrolysis temperature. At different temperatures, the increase in PA6 ratio showed an opposite trend to the yield, which indicates that cellulose plays a dominant role in the yield. Generation of caprolactam monomer is the main process of PA6 pyrolysis. Comparing the theoretical char yield values calculated using equation (6) with the experiment values, it can be seen from **Figure 4(b-d)** that the solid char yields of each ratio are higher than the theoretical values, which indicates that a synergistic effect between CE and PA6 occurs, probably the presence of CE induces a cross-linking reaction of PA6, which produces a considerable amount of char or residual material (Bakirtzis *et al.* 2014). Among the above ratios, when CE/PA6 is 5/5, the difference between theoretical and actual yield is the largest, indicating that the synergistic effect is the best under this ratio.

3.2. Effect of the synergistic reaction on the adsorption of Cr(VI)

3.2.1. Adsorption capacity

Figure 5(a) demonstrates the adsorption of Cr(VI) on solid carbon with different ratios at 700°C. From the figure, it can be observed that the highest adsorption capacity of C5A5C for Cr(VI) was observed, i.e., the best effect was achieved when PA6/CE was 5/5, and the adsorption capacity reached 59.04 mg/g, which was 98.3% and 34.5% higher than that of CPA6(29.78 mg/g) and CCE(43.91mg/g), respectively, which indicated that co-pyrolysis improved the adsorption capacity of the char. **Figure 5(b)** shows the tests at different temperatures for this ratio. The best adsorption performance for Cr(VI) was achieved with solid carbon generated at 700°C, indicating that temperature plays a key role in increasing carbon adsorption performance.

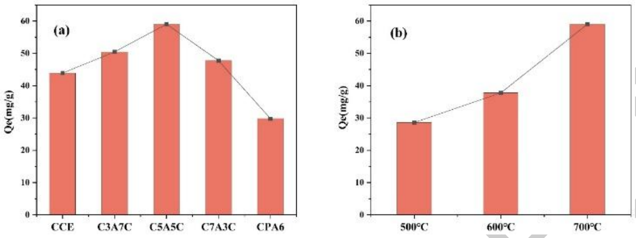

Figure 5. (a) Adsorption of different ratios of solid biochar (700°C); (b) Adsorption of solid biochar at different temperatures of 5A5C

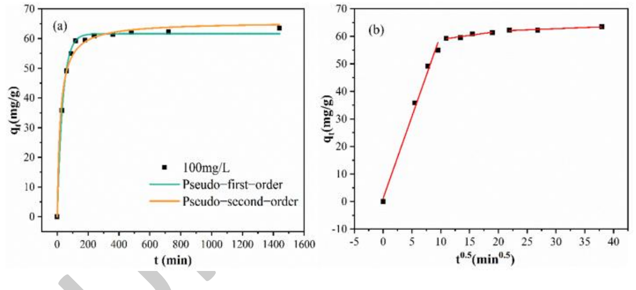

Figure 6. (a) Proposed primary and proposed secondary kinetic models for Cr(VI) adsorption by C5A5C; (b) Intra-particle diffusion model

3.2.2. Adsorption kinetics

The kinetic parameters of the PFO, PSO, and IPD models obtained by fitting the adsorption data of Cr(VI) on pyrolytic carbon C5A5C using the pseudo-first-order kinetic model, pseudo-second-order kinetic model, and intra-particle diffusion kinetic model are shown in **Table 1**, and the fitting results are illustrated in **Figure 6**. As shown in **Figure 6(a)**, the adsorption rate of Cr(VI) ions by C5A5C is extremely fast in the first 60 minutes, indicating that Cr(VI) binds smoothly to the active sites on the C5A5C surface, thereby shortening the reaction time. Subsequently, the adsorption rate slows down, and the adsorption capacity gradually approaches saturation, indicating that there are almost no vacant binding sites at this point. The adsorption experiment gradually reaches equilibrium after 240 minutes. The kinetic correlation coefficient R^2 in **Table S1** shows that the R^2 value (0.99662) of the fitted second-order kinetic model is significantly better than the R^2 value (0.99178) of the fitted first-order kinetic model, and the theoretical adsorption capacity (65.6 mg/g) is closer to the experimental value (64.6 mg/g), indicating that the adsorption behavior of C5A5C is better described by the pseudo-second-order kinetic model, and adsorption may be regulated by chemical interactions (Lv *et al.* 2021). The internal diffusion model was used to further elucidate the adsorption process. As shown in **Table S1**, the C value of the fitting results is not zero, and the model in **Figure 6(b)** also exhibits three steps, indicating that the adsorption of Cr(VI) by C5A5C involves multiple stages. The first stage has the highest k1 value, involving the diffusion of Cr(VI) from the liquid phase to the outer surface of C5A5C, which is the fastest process. In the second stage, the pollutant migrates from the outer surface of the carbon through the pores to the inner layers. The third stage has an extremely low k value, with adsorption gradually approaching equilibrium (Ke *et al.* 2022).

3.2.3. Adsorption behavior

The chemical properties of the material surface were observed by XPS and the main elements tested in the total spectrum were C, O, N and Cr (**Figure 7(a)**). The Cr signal detected on the spectrum showed two peaks attributed to Cr2p3 at 577.36 eV and Cr2p1 at 587.29 eV. Indicates the presence of chromium on the surface of biochar and a change in the valence state of chromium (Xu *et al.* 2019). The high-resolution XPS spectrum of Cr2p adsorbed on C5A5C for Cr(VI) is shown in **Figure 7(b)**, in which both Cr2p3 and Cr2p1 can be convolved into two peaks, with the peaks at 577.09 eV and 586.17 eV for Cr(III), and the peaks at 577.77 eV and 587.29 eV for Cr(VI). The coexistence of Cr(III) and Cr(VI) indicates that the removal of Cr(VI) by C5A5C involves both adsorption and reduction processes. The N1s adsorption contrast spectrum of C5A5C (**Figure 7(c)**) confirms that nitrogen-containing functional groups contribute to the formation of hydrogen bonds. (Cheng *et al.* 2022). The characteristic peaks of -NH_2/N-H and -NH_3^+ were 398.77 eV and 401.48 eV before adsorption and 398.27 eV and 401.22 eV after contacting with Cr(VI), respectively, indicating that hydrogen bonding was involved in the adsorption process (Ahmed *et al.* 2022). The asymmetric O1s spectra (**Figure 7(d)**) on C5A5C can be subdivided into C-O (533.28 eV), O-H (532.36 eV), and C=O (531.58 eV), and their intensities reflect the abundance of surface functional groups (Elmouwahidi *et al.* 2017; Rosas *et al.* 2012; Tsaneva *et al.* 2014). The peak position of O-H after adsorption of Cr(VI) was significantly shifted to 532.08eV, indicating the formation of hydrogen bond between -OH group and C5A5C (Gao *et al.* 2022). In addition, the reduction of -OH and C=O binding energies reveals the direction of valence bond electron transfer during adsorption (e.g., Eqs. (8) - (9)) and suggests that O atoms provide electrons in the reduction of Cr(VI) by C5A5C (Li *et al.* 2019). The Cr-O morphology of C5A5C-Cr at 530.18 eV also proves the reduction reaction. The above findings indicate that the increase in the removal of chromium (VI) is due to the provision of electrons by the functional groups, resulting in a reduction reaction.

Table 1. Kinetic model fitting parameters for C5A5C adsorption of Cr(VI).

Kinetic model	Parameters	Values
Pseudo–first–order	q_e	61.628
	k1	0.02739
	R^2	0.99178
Pseudo–second–order	q_e	65.6
	k2	7.41373E-4
	R^2	0.99662
Intra–particle diffusion	ki,1	5.94906
	C	1.21034
	R^2	0.99099
	ki,2	0.28995
	C	55.9973
	R^2	0.89811
	ki,3	0.08419
	C	60.24988
	R^2	0.8889

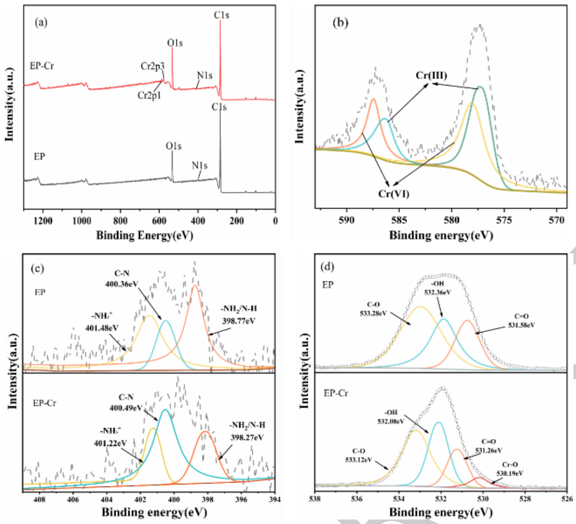

Figure 7. XPS survey spectra (a); After adsorption, high-resolution Cr2p (b)Spectra N1s (c) and O1s (d) before and after C5A5C adsorption

$$\text{C-OH+Cr}(\text{VI}) \rightarrow \text{C=O+Cr}(\text{III}) \tag{8}$$

$$\text{C=O+Cr}(\text{VI}) \rightarrow \text{-COOH+Cr}(\text{III}) \tag{9}$$

3.3. Synergistic mechanism

3.3.1. Surface functional groups analysis

Figure 8(a-e) demonstrates the FTIR spectra of CCE, C3A7C, C5A5C, C7A3C, and CPA6. It can be seen that CCE has characteristic absorption bands at 3394 cm^{-1} (-OH stretching), 1620 cm^{-1} (C=C stretching, C=O stretching) and 1440 cm^{-1} (-COOH stretching) (Melo *et al.* 2020). The characteristic peaks of CPA6 are located at 3405 cm^{-1} (N-H stretching), 1633 cm^{-1} (C=O stretching), 1425 cm^{-1} (-CH2 bending) and 426 cm^{-1} (N-H stretching) (Lin *et al.* 2020; Y. Liu *et al.* 2021). In the copolymer, a CPA6-specific absorption band was observed at 430 cm^{-1} (Ma *et al.* 2016). However, we noticed that the peaks corresponding to N-H and C=O were shifted when cellulose and PA6 were mixed, suggesting that the amide (N-H and C=O) functional groups in CPA6 may react with the OH functional groups on the cellulose surface. (de Matos Costa *et al.* 2021). Whereas, the peak intensities of -OH and -COOH groups improved considerably with the addition of PA6, as can be clearly observed for C5C5C (**Figure 8(c)**). **Figure 8(f)** shows the adsorption of Cr(VI) by C5A5C. It is clearly apparent that the strengths of -OH and -COOH groups were substantially distorted before and after the adsorption, and they may be implicated in the adsorption reaction process of Cr (Pannase *et al.* 2020). The changes of these peaks confirmed that the functional groups played a major role in the degradation of Cr(VI).

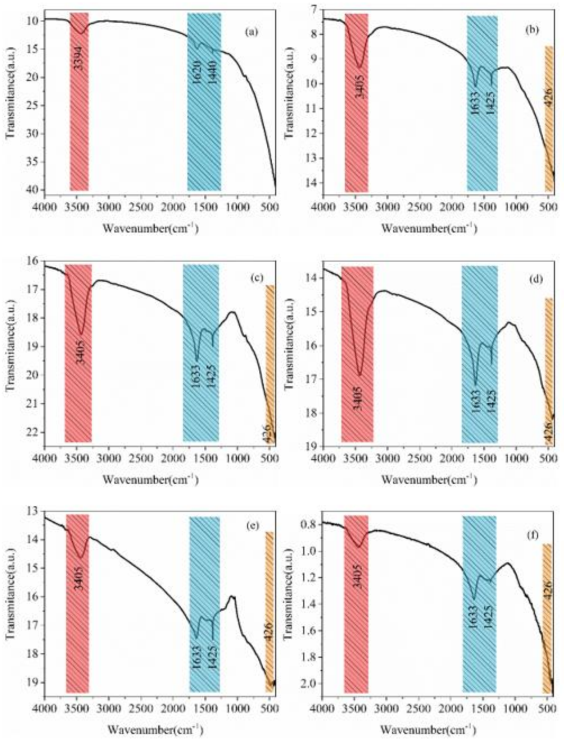

Figure 8. FTIR of (a)CCE, (b)C3A7C, (c)C5A5C, (d)C7A3C, (e)CPA6 and(f) C5A5C-Cr

3.3.2. Specific surface area and pore volume analysis

The surface characteristics of 700°C pyrolyzed biochar are shown in **Figure 9**. The BET data, the pore volume (PV), the specific surface area and the average pore diameter(APD) of CCE, C3A7C, C5A5C and C7A3C are shown in **Table 2**. The pore volume of the pyrolyzed biochar increased and then decreased with the increase of the proportion of PA6, and the best result was obtained when the proportion was 50%. The specific surface area of pyrolytic carbon has a significant advantage over CCE at 50% PA6 content. The analysis shows that the pore volume and specific surface area of solid biochar are optimal when CE/PA6 is 5/5.

Table 2. BET results of CCE, C3A7C, C5A5C and C7A3C

Sample	BET(m²/g)	SSA(m²/g)	PV(cm3/g)	APD(nm)
CCE	0.7476	0.8220	0.000000	0.7941
C3A7C	0.2932	0.3040	0.000755	0.7813
C5A5C	0.9717	1.0341	0.001690	0.7953
C7A3C	0.5882	0.5184	0.000989	3.5005

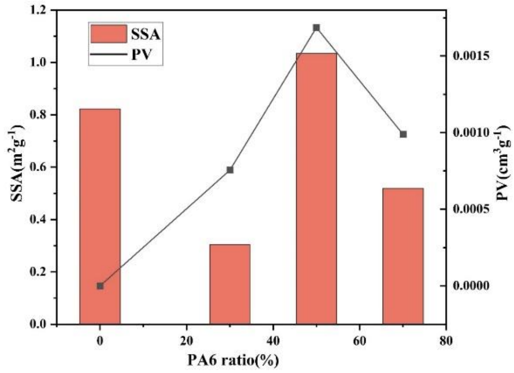

Figure 9. SSA/PV of different ratios of solid biochar (700°C)

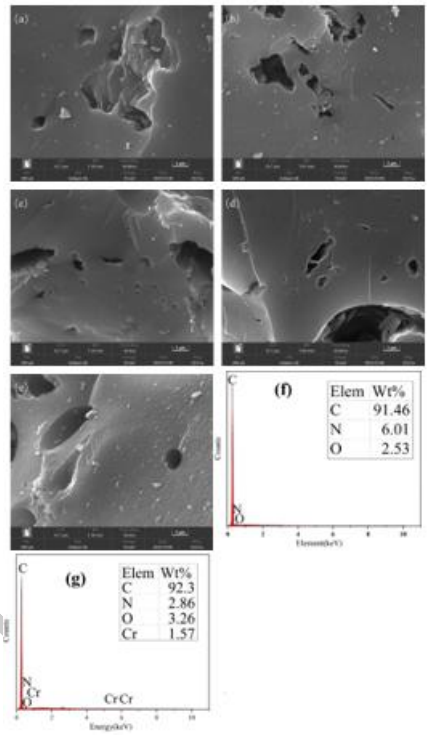

Figure 10. SEM of (a)CCE, (b)C3A7C, (c)C5A5C, (d)C7A3C and (e)CPA6; (f) EDS energy spectra of C5A5C and (g) C5A5C-Cr

3.3.3. Surface morphology analysis

Scanning electron microscopy was used to investigate the surface morphology of solid carbon at various ratios (700°C). CCE has a rough surface (**Figure 10a**) with fewer pores, whereas the solid carbon pores increase with the addition of PA6 (**Figure 10b-e**), with the small pores of C5A5C being particularly prominent. This suggests that the introduction of PA6 facilitated the formation of pores, possibly due to the decomposition and volatilization of organic materials or the generation of flammable gases during the carbonization process (Flanagan *et al.* 2012). In addition, the EDS spectra showed that the C5A5C-Cr surface leaked chromium signals, indicating that chromium had been successfully loaded onto the carbon surface (**Figure 10f-g**).

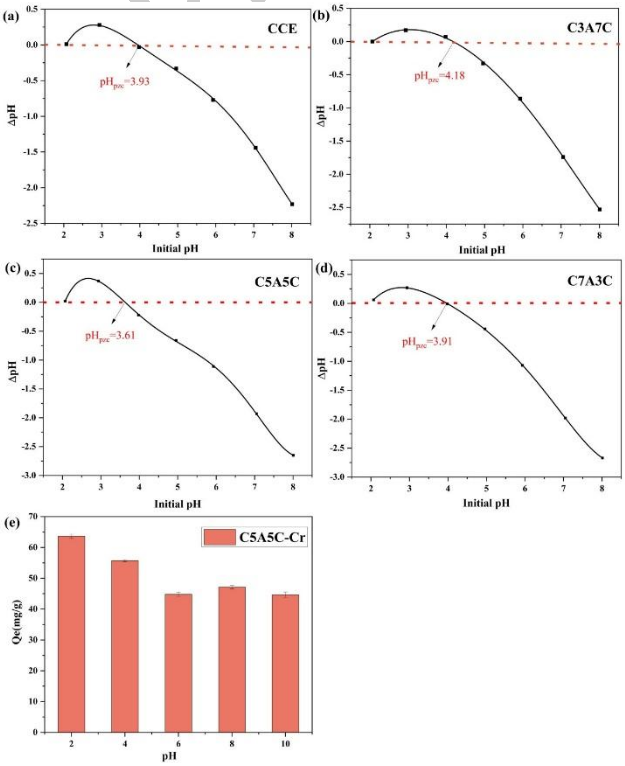

Figure 11. pH_{PZC} measurement curves for each material(a-d); (e)Effect of pH on the adsorption of Cr(VI) by C5A5C

3.3.4. Surface charge analysis

An important characteristic that affects anion adsorption is the pHpzc value of the adsorbent. The zero-point charge can reflect the surface charge state of the adsorbent. When the zero-point charge of the material is greater than the pH of the solution, the surface is positively charged, and the charge decreases with increasing pH (Zyoud *et al.* 2019). As shown in **Figure 11**, the experimental pHpzc values for CCE, C3A7C, C5A5C and C7A3C were 3.93, 4.18, 3.61 and 3.91, respectively. It may be that with a CE/PA6 of 5/5, more acidic oxygen species are produced by pyrolysis (Menéndez *et al.*1999; Mokrzycki *et al.* 2022), and thus C5A5C has the lowest pHpzc value. The optimum adsorption condition for Cr(VI) by C5A5C was pH=2, at which time the adsorption capacity was 63.6 mg/g. The adsorption of C5A5C showed an opposite trend with increasing initial pH. This suggests that the surface is positively charged at solution pH around 2-3, possibly due to surface protonation (Carraro *et al.* 2019). However, the main forms of hexavalent chromium in solution are negatively charged CrO_4^{2-} and $HCrO_4^-$, so the biochar material adsorbs the negatively charged ions by electrostatic action. As the pH increases, the surface of C5A5C is negatively charged and the adsorption performance deteriorates due to electrostatic interaction (Garg *et al.* 2007). **Figure 12** illustrates the synergistic interaction mechanism between CE and PA6.

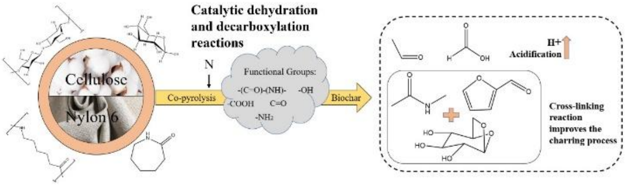

Figure 12. The synergistic effect between CE and PA6 in co-pyrolysis

4. Conclusions

The study confirmed the synergistic effect of CE and PA6 in the co-pyrolysis process and evaluated the adsorption capacity of solid carbon for Cr(VI). From the thermogravimetric results, the synergistic effect of CE and PA6 is obvious, with the strongest synergistic effect produced when the PA6 content is 50%. The presence of CE induced a cross-linking reaction in PA6, producing a considerable amount of char or residue. During decomposition at 700°C, the incorporation of PA6 promotes the formation of pores and improves the specific surface area and pore volume. In addition, the synergistic effect changes the zero-point charge of the material and promotes the reaction of surface functional groups. The creation of H-bonds and the role of -OH and -COOH groups contribute significantly to the adsorption of Cr(VI) by C5A5C. This work proved the interaction of CE and PA6 during pyrolysis and proposed novel ways and concepts for treating blends and removing Cr(VI).

Acknowledgements

This research was supported by National Natural Science Foundation of China (No.52100161). The authors would like to thank reviewers for commenting on this paper.

References

Ahmed, I., Hasan, Z., Lee, G., Lee, H. J., & Jhung, S. H. (2022). Contribution of hydrogen bonding to liquid-phase adsorptive removal of hazardous organics with metal-organic framework-based materials. *Chemical Engineering Journal, 430*, 132596. doi: https://doi.org/10.1016/j.cej.2021.132596

Bakirtzis, D., Ramani, A., Zhang, J., & Delichatsios, M. A. (2014). Simplified structure of the condensed phase of fire retarded PA6 nanocomposites in TGA as related flammability. *Fire Safety Journal, 69*, 69-75. doi: 10.1016/j.firesaf.2014.08.006

Ball, R., McIntosh, A. C., & Brindley, J. (2007). Feedback processes in cellulose thermal decomposition: implications for fire-retarding strategies and treatments. *Combustion Theory and Modelling, 8*(2), 281-291. doi: 10.1088/1364-7830/8/2/005

Bozi, J., Mihályi, M. R., & Blazsó, M. (2013). Study on temperature dependence of catalytic thermal decomposition of polyamides and polyurethanes mixed with acidic zeolites. *Journal of Analytical and Applied Pyrolysis, 101*, 103-110. doi: 10.1016/j.jaap.2013.02.005

Carraro, P. S., Spessato, L., Crespo, L. H. S., Yokoyama, J. T. C., Fonseca, J. M., Bedin, K. C., . . . Almeida, V. C. (2019). Activated carbon fibers prepared from cellulose and polyester–derived residues and their application on removal of Pb2+ ions from aqueous solution. *Journal of Molecular Liquids, 289*, 111150. doi: https://doi.org/10.1016/j.molliq.2019.111150

Cheng, Y., Wang, B., Shen, J., Yan, P., Kang, J., Wang, W., . . . Chen, Z. (2022). Preparation of novel N-doped biochar and its high adsorption capacity for atrazine based on π–π electron donor-acceptor interaction. *Journal of Hazardous Materials, 432*, 128757. doi: https://doi.org/10.1016/j.jhazmat.2022.128757

Dai, Q., Liu, Q., Zhang, X., Cao, L., Hu, B., Shao, J., . . . Gao, B. (2022). Synergetic effect of co-pyrolysis of sewage sludge and lignin on biochar production and adsorption of methylene blue. *Fuel, 324*. doi: 10.1016/j.fuel.2022.124587

Dai, Q., Xiang, W., Liu, Q., Wang, M., & Zhang, X. (2022). Co-pyrolysis biochar derived from sewage sludge and lignin: Synergetic effect and adsorption properties. *Journal of Environmental Chemical Engineering, 10*(3). doi: 10.1016/j.jece.2022.107898

de Matos Costa, A. R., Lima, J. C., dos Santos, R., Barreto, L. S., Henrique, M. A., de Carvalho, L. H., & de Almeida, Y. M. B. (2021). Rheological, thermal and morphological properties of polyethylene terephthalate/polyamide 6/rice husk ash composites. *Journal of Applied Polymer Science, 138*(36). doi: 10.1002/app.50916

de Rezende Locatel, W., Mohabeer, C., Laurenti, D., Schuurman, Y., & Guilhaume, N. (2022). Co-pyrolysis of beech wood and polyamide-6: Effect of HZSM-5 catalyst on the properties of pyrolysis oils. *Journal of Analytical and Applied Pyrolysis, 167*. doi: 10.1016/j.jaap.2022.105696

Elmouwahidi, A., Bailón-García, E., Pérez-Cadenas, A. F., Maldonado-Hódar, F. J., & Carrasco-Marín, F. (2017). Activated carbons from KOH and H 3 PO 4 -activation of olive residues and its application as supercapacitor electrodes. *Electrochimica Acta, 229*, 219-228. doi: 10.1016/j.electacta.2017.01.152

Espinoza Pérez, L. A., Espinoza Pérez, A. T., & Vásquez, Ó. C. (2022). Exploring an alternative to the Chilean textile waste: A carbon footprint assessment of a textile recycling process. *Science of The Total Environment, 830*. doi: 10.1016/j.scitotenv.2022.154542

Flanagan, J. C. A., Dornan, L. M., McLaughlin, M. G., McCreanor, N. G., Cook, M. J., & Muldoon, M. J. (2012). The synthesis of N-heterocycles via copper/TEMPO catalysed aerobic oxidation of amino alcohols. *Green Chemistry, 14*(5). doi: 10.1039/c2gc35062a

Gao, T., Shi, W., Zhao, M., Huang, Z., Liu, X., & Ruan, W. (2022). Preparation of spiramycin fermentation residue derived biochar for effective adsorption of spiramycin from wastewater. *Chemosphere, 296*, 133902. doi: https://doi.org/10.1016/j.chemosphere.2022.133902

Garg, U. K., Kaur, M. P., Garg, V. K., & Sud, D. (2007). Removal of hexavalent chromium from aqueous solution by agricultural waste biomass. *Journal of Hazardous Materials, 140*(1), 60-68. doi: https://doi.org/10.1016/j.jhazmat.2006.06.056

Han, L., Li, J., Qu, C., Shao, Z., Yu, T., & Yang, B. (2022). Recent Progress in Sludge Co-Pyrolysis Technology. *Sustainability, 14*(13). doi: 10.3390/su14137574

Hanoğlu, A., Çay, A., & Yanık, J. (2019). Production of biochars from textile fibres through torrefaction and their characterisation. *Energy, 166*, 664-673. doi: 10.1016/j.energy.2018.10.123

Haslinger, S., Hummel, M., Anghelescu-Hakala, A., Maattanen, M., & Sixta, H. (2019). Upcycling of cotton polyester blended textile waste to new man-made cellulose fibers. *Waste Manag, 97*, 88-96. doi: 10.1016/j.wasman.2019.07.040

Holland, C., Numata, K., Rnjak-Kovacina, J., & Seib, F. P. (2018). The Biomedical Use of Silk: Past, Present, Future. *Advanced Healthcare Materials, 8*(1). doi: 10.1002/adhm.201800465

Kankia, M. U., Baloo, L., Danlami, N., Mohammed, B. S., Haruna, S., Abubakar, M., . . . Salihi, I. U. (2021). Performance of Fly Ash-Based Inorganic Polymer Mortar with Petroleum Sludge Ash. Polymers, 13(23). doi: 10.3390/polym13234143

Kankia, M. U., Baloo, L., Danlami, N., Samahani, W. N., Mohammed, B. S., Haruna, S., . . . Amila Bt Wan Zawawi, N. (2021). Optimization of Cement-Based Mortar Containing Oily Sludge Ash by Response Surface Methodology. Materials, 14(21). doi: 10.3390/ma14216308

Kasavan, S., Yusoff, S., Guan, N. C., Zaman, N. S. K., & Fakri, M. F. R. (2021). Global trends of textile waste research from 2005 to 2020 using bibliometric analysis. *ENVIRONMENTAL SCIENCE AND POLLUTION RESEARCH, 28*(33), 44780-44794. doi: 10.1007/s11356-021-15303-5

Ke, Z., Mei, M., Liu, J., Du, P., Zhang, B., Wang, T., . . . Li, J. (2022). Deep eutectic solvent assisted facile and efficient synthesis of nitrogen-doped magnetic biochar for hexavalent chromium elimination: Mechanism and performance insights. Journal of Cleaner Production, 357, 132012. doi: https://doi.org/10.1016/j.jclepro.2022.132012

Kumar, A., & Samadder, S. R. (2017). A review on technological options of waste to energy for effective management of municipal solid waste. *Waste Manag, 69*, 407-422. doi: 10.1016/j.wasman.2017.08.046

Lee, H. S., Jung, S., Lin, K.-Y. A., Kwon, E. E., & Lee, J. (2023). Upcycling textile waste using pyrolysis process. *SCIENCE OF THE TOTAL ENVIRONMENT, 859*. doi: 10.1016/j.scitotenv.2022.160393

Li, P., Fu, T., Gao, X., Zhu, W., Han, C., Liu, N., . . . Ma, W. (2019). Adsorption and Reduction Transformation Behaviors of Cr(VI) on Mesoporous Polydopamine/Titanium Dioxide Composite Nanospheres. *Journal of Chemical & Engineering Data, 64*(6), 2686-2696. doi: 10.1021/acs.jced.9b00111

Lin, X., Liu, Y., Chen, X., Wu, Y., Cui, L., Mao, L., . . . Lin, M. (2020). Reactive Compatibilization of Polyamide 6/Olefin Block Copolymer Blends: Phase Morphology, Rheological Behavior, Thermal Behavior, and Mechanical Properties. *Materials, 13*(5). doi: 10.3390/ma13051146

Liu, L., Liu, X., Wang, D., Lin, H., & Huang, L. (2020). Removal and reduction of Cr(VI) in simulated wastewater using magnetic biochar prepared by co-pyrolysis of nano-zero-valent iron and sewage sludge. Journal of Cleaner Production, 257, 120562. doi: https://doi.org/10.1016/j.jclepro.2020.120562

Liu, J., Yang, X., Liu, H., Jia, X., & Bao, Y. (2021). Mixed biochar obtained by the co-pyrolysis of shrimp shell with corn straw: Co-pyrolysis characteristics and its adsorption capability. *Chemosphere, 282*, 131116. doi: 10.1016/j.chemosphere.2021.131116

Liu, Y., Jiang, S., Yan, W., Qin, J., He, M., Qin, S., & Yu, J. (2021). Enhanced mechanical and thermal properties of polyamide 6/p (N-(4-F-phenylmaleimide)–alt-styrene) composites based on interfacial complexation inducing crystal transformation. *Polymer, 214*, 123237. doi: https://doi.org/10.1016/j.polymer.2020.123237

Lu, L., Fan, W., Ge, S., Liew, R. K., Shi, Y., Dou, H., . . . Lam, S. S. (2022). Progress in recycling and valorization of waste silk. *Science of The Total Environment, 830*. doi: 10.1016/j.scitotenv.2022.154812

Lv, M., Li, D., Zhang, Z., Logan, B. E., Liu, G., Sun, M., . . . Feng, Y. (2021). Unveiling the correlation of Fe3O4 fractions upon the adsorption behavior of sulfamethoxazole on magnetic activated carbon. Science of The Total Environment, 757, 143717. doi: https://doi.org/10.1016/j.scitotenv.2020.143717

Ma, Y., Zhou, T., Su, G., Li, Y., & Zhang, A. (2016). Understanding the crystallization behavior of polyamide 6/polyamide 66 alloys from the perspective of hydrogen bonds: projection moving-window 2D correlation FTIR spectroscopy and the enthalpy. *RSC Advances, 6*(90), 87405-87415. doi: 10.1039/c6ra09611e

Melo, R. P., Rosa, M. P. d., Beck, P. H., Tienne, L. G. P., & Marques, M. d. F. V. (2020). Thermal, morphological and mechanical properties of composites based on polyamide 6 with cellulose, silica and their hybrids from rice husk. *Journal of Composite Materials, 55*(13), 1811-1821. doi: 10.1177/0021998320978290

Menéndez, J. A., Menéndez, E. M., Iglesias, M. J., García, A., & Pis, J. J. (1999). Modification of the surface chemistry of active carbons by means of microwave-induced treatments. *Carbon, 37*(7), 1115-1121. doi: https://doi.org/10.1016/S0008-6223(98)00302-9

Mohd Hanafiah, Z., Wan Mohtar, W. H. M., Rohani, R., Fadzizi, M. F., Wan-Mohtar, W. A. A.-Q. I., Sayed, K., . . . Indarto, A. (2024). Removal of pharmaceutical compounds from sewage effluent by the nanofiltration membrane. Journal of Water Process Engineering, 68, 106320. doi: https://doi.org/10.1016/j.jwpe.2024.106320

Mohd Hanafiah, Z., Wan Mohtar, W. H. M., Wan-Mohtar, W. A. A. Q. I., Bithi, A. S., Rohani, R., Indarto, A., . . . Binti Abdul Manan, T. S. (2024). Removal of pharmaceutical compounds and toxicology study in wastewater using Malaysian fungal Ganoderma lucidum. Chemosphere, 358, 142209. doi: https://doi.org/10.1016/j.chemosphere.2024.142209

Mokrzycki, J., Fedyna, M., Marzec, M., Szerement, J., Panek, R., Klimek, A., . . . Mierzwa-Hersztek, M. (2022). Copper ion-exchanged zeolite X from fly ash as an efficient adsorbent of phosphate ions from aqueous solutions. *Journal of Environmental Chemical Engineering, 10*(6), 108567. doi: https://doi.org/10.1016/j.jece.2022.108567

Mu, L., Chen, J., Yao, P., Zhou, D., Zhao, L., & Yin, H. (2016). Evaluation of co-pyrolysis petrochemical wastewater sludge with lignite in a thermogravimetric analyzer and a packed-bed reactor: Pyrolysis characteristics, kinetics, and products analysis. *Bioresource Technology, 221*, 147-156. doi: 10.1016/j.biortech.2016.09.011

Pannase, A. M., Singh, R. K., Ruj, B., & Gupta, P. (2020). Decomposition of polyamide via slow pyrolysis: Effect of heating rate and operating temperature on product yield and composition. *Journal of Analytical and Applied Pyrolysis, 151*. doi: 10.1016/j.jaap.2020.104886

Perez, B. A., Jayarama Krishna, J. V., & Toraman, H. E. (2023). Insights into co-pyrolysis of polyethylene terephthalate and polyamide 6 mixture through experiments, kinetic modeling and machine learning. *Chemical Engineering Journal, 468*. doi: 10.1016/j.cej.2023.143637

Rangasamy, G., Mani, S., Senathipathygoundar Kolandavelu, S. K., Alsoufi, M. S., Mahmoud Ibrahim, A. M., Muthusamy, S., . . . Elsheikh, A. H. (2021). An extensive analysis of mechanical, thermal and physical properties of jute fiber composites with different fiber orientations. *Case Studies in Thermal Engineering, 28*. doi: 10.1016/j.csite.2021.101612

Rosas, J. M., Ruiz-Rosas, R., Rodríguez-Mirasol, J., & Cordero, T. (2012). Kinetic study of the oxidation resistance of phosphorus-containing activated carbons. *Carbon, 50*(4), 1523-1537. doi: 10.1016/j.carbon.2011.11.030

Salman, B., Ong, M. Y., Nomanbhay, S., Salema, A. A., Sankaran, R., & Show, P. L. (2019). Thermal Analysis of Nigerian Oil Palm Biomass with Sachet-Water Plastic Wastes for Sustainable Production of Biofuel. *Processes, 7*(7). doi: 10.3390/pr7070475

Sayed, K., Baloo, L., Kutty, S. R. B. M., Al Madhoun, W., Kankia, M. U., Jagaba, A. H., & Singa, P. K. (2022). Optimization of palm oil mill effluent final discharge as biostimulant for biodegradation of tapis light crude petroleum oil in seawater. Journal of Sea Research, 188, 102268. doi: https://doi.org/10.1016/j.seares.2022.102268

Sayed, K., Baloo, L., Kutty, S. R. B. M., & Makba, F. (2021). Potential biodegradation of Tapis Light Crude Petroleum Oil, using palm oil mill effluent final discharge as biostimulant for isolated halotolerant Bacillus strains. Marine Pollution Bulletin, 172, 112863. doi: https://doi.org/10.1016/j.marpolbul.2021.112863

Sayed, K., Wan Mohtar, W. H. M., Hanafiah, Z. M., Wan-Mohtar, W. A. A. Q. I., Abd Manan, T. S. B., & Mohamad Sharif, S. A. B. (2024). Simultaneous enhanced removal of pharmaceuticals and hormone from wastewaters using series combinations of ultra-violet irradiation, bioremediation, and adsorption technologies. Journal of Water Process Engineering, 57, 104589. doi: https://doi.org/10.1016/j.jwpe.2023.104589

Singh, S., Patil, T., Tekade, S. P., Gawande, M. B., & Sawarkar, A. N. (2021). Studies on individual pyrolysis and co-pyrolysis of corn cob and polyethylene: Thermal degradation behavior, possible synergism, kinetics, and thermodynamic analysis. *Science of The Total Environment, 783*. doi: 10.1016/j.scitotenv.2021.147004

Stanescu, M. D. (2021). State of the art of post-consumer textile waste upcycling to reach the zero waste milestone. *ENVIRONMENTAL SCIENCE AND POLLUTION RESEARCH, 28*(12), 14253-14270. doi: 10.1007/s11356-021-12416-9

Sun, L., Wang, H., Li, W., Zhang, J., Zhang, Z., Lu, Z., . . . Dong, C. (2021). Preparation, characterization and testing of flame retardant cotton cellulose material: flame retardancy, thermal stability and flame-retardant mechanism. *Cellulose, 28*(6), 3789-3805. doi: 10.1007/s10570-020-03632-6

To, M. H., Uisan, K., Ok, Y. S., Pleissner, D., & Lin, C. S. K. (2019). Recent trends in green and sustainable chemistry: rethinking textile waste in a circular economy. *Current Opinion in Green and Sustainable Chemistry, 20*, 1-10. doi: 10.1016/j.cogsc.2019.06.002

Tsaneva, V. N., Kwapinski, W., Teng, X., & Glowacki, B. A. (2014). Assessment of the structural evolution of carbons from microwave plasma natural gas reforming and biomass pyrolysis using Raman spectroscopy. *Carbon, 80*, 617-628. doi: 10.1016/j.carbon.2014.09.005

Wang, X., Deng, S., Tan, H., Adeosun, A., Vujanović, M., Yang, F., & Duić, N. (2016). Synergetic effect of sewage sludge and biomass co-pyrolysis: A combined study in thermogravimetric analyzer and a fixed bed reactor. *Energy Conversion and Management, 118*, 399-405. doi: 10.1016/j.enconman.2016.04.014

Wang, Y., Yang, Q., Chen, J., Yang, J., Zhang, Y., Chen, Y., . . . Chang, J. S. (2020). Adsorption behavior of Cr(VI) by magnetically modified Enteromorpha prolifera based biochar and the toxicity analysis. *J Hazard Mater, 395*, 122658. doi: 10.1016/j.jhazmat.2020.122658

Xu, Z., Tian, D., Sun, Z., Zhang, D., Zhou, Y., Chen, W., & Deng, H. (2019). Highly porous activated carbon synthesized by pyrolysis of polyester fabric wastes with different iron salts: Pore development and adsorption behavior. Colloids and Surfaces A: Physicochemical and Engineering Aspects, 565, 180-187. doi: https://doi.org/10.1016/j.colsurfa.2019.01.007

Xu, Z., Yuan, Z., Zhang, D., Huang, Y., Chen, W., Sun, Z., & Zhou, Y. (2019). Cr(VI) removal with rapid and superior performance utilizing cost-efficient waste-polyester-textile-based mesoporous carbon: Behavior and mechanism. *Journal of Molecular Liquids, 278*, 496-504. doi: 10.1016/j.molliq.2019.01.088

Yang, H., Yan, R., Chen, H., Lee, D. H., & Zheng, C. (2007). Characteristics of hemicellulose, cellulose and lignin pyrolysis. *Fuel, 86*(12), 1781-1788. doi: https://doi.org/10.1016/j.fuel.2006.12.013

Zeng, H., Qi, W., Zhai, L., Wang, F., Zhang, J., & Li, D. (2021). Magnetic biochar synthesized with waterworks sludge and sewage sludge and its potential for methylene blue removal. *Journal of Environmental Chemical Engineering, 9*(5). doi: 10.1016/j.jece.2021.105951

Zhang, X., Lv, L., Qin, Y., Xu, M., Jia, X., & Chen, Z. (2018). Removal of aqueous Cr(VI) by a magnetic biochar derived from Melia azedarach wood. *Bioresour Technol, 2ner56*, 1-10. doi: 10.1016/j.biortech.2018.01.145

Zhu, P., Sui, S., Wang, B., Sun, K., & Sun, G. (2004). A study of pyrolysis and pyrolysis products of flame-retardant cotton fabrics by DSC, TGA, and PY–GC–MS. *Journal of Analytical and Applied Pyrolysis, 71*(2), 645-655. doi: 10.1016/j.jaap.2003.09.005

Zyoud, A. H., Zubi, A., Zyoud, S. H., Hilal, M. H., Zyoud, S., Qamhieh, N., . . . Hilal, H. S. (2019). Kaolin-supported ZnO nanoparticle catalysts in self-sensitized tetracycline photodegradation: Zero-point charge and pH effects. *Applied Clay Science, 182*, 105294. doi: https://doi.org/10.1016/j.clay.2019.105294